



PAPER • OPEN ACCESS

Analysis of two-color photoelectron spectroscopy for attosecond metrology at seeded free-electron lasers

To cite this article: P K Maroju *et al* 2021 *New J. Phys.* **23** 043046

View the [article online](#) for updates and enhancements.

You may also like

- [Attosecond laser station](#)
Hao Teng, , Xin-Kui He et al.
- [Attosecond technology\(ies\) and science](#)
Jens Biegert, Francesca Calegari, Nirit Dudovich et al.
- [Introduction to attosecond delays in photoionization](#)
J M Dahlström, A L'Huillier and A Maquet



PAPER

Analysis of two-color photoelectron spectroscopy for attosecond metrology at seeded free-electron lasers

OPEN ACCESS

RECEIVED

27 October 2020

REVISED

12 March 2021

ACCEPTED FOR PUBLICATION

16 March 2021

PUBLISHED

23 April 2021

Original content from this work may be used under the terms of the [Creative Commons Attribution 4.0 licence](#).

Any further distribution of this work must maintain attribution to the author(s) and the title of the work, journal citation and DOI.



P K Maroju¹, C Grazioli², M Di Fraia³, M Moioli¹, D Ertel¹, H Ahmadi¹, O Plekan³, P Finetti³, E Allaria^{3,16}, L Giannessi^{3,4}, G De Ninno^{3,5}, S Spampinati³, A A Lutman⁶, R J Squibb⁷, R Feifel⁷, P Carpeggiani⁸, M Reduzzi⁹, T Mazza¹⁰, M Meyer¹⁰, S Bengtsson¹¹, N Ibrakovic¹¹, E R Simpson¹¹, J Mauritsson¹¹, T Csizmadia¹², M Dumergue¹², S Kühn¹², N G Harshitha¹², D You¹³, K Ueda¹³, M Labeye¹⁴, J E Bækthøj¹⁴, K J Schafer¹⁴, E V Gryzlova¹⁵, A N Grum-Grzhimailo¹⁵, K C Prince³, C Callegari³ and G Sansone^{1,*}

¹ Physikalisches Institut, Albert-Ludwigs-Universität, Stefan Meier Strasse 19, 79104 Freiburg, Germany

² ISM-CNR, Trieste LD2 Unit, Basovizza AREA Science Park, Trieste, I-34149, Italy

³ Elettra-Sincrotrone Trieste, 34149 Basovizza, Trieste, Italy

⁴ ENEA C.R. Frascati, Via E. Fermi 45, 00044 Frascati, Italy

⁵ Laboratory of Quantum Optics, University of Nova Gorica, 5001 Nova Gorica, Slovenia

⁶ SLAC National Accelerator Laboratory, Menlo Park, California 94025, United States of America

⁷ Department of Physics, University of Gothenburg, Origovägen 6B, 412 96 Gothenburg, Sweden

⁸ Technische Universität Wien, Austria

⁹ Dipartimento Fisica Politecnico, Piazza Leonardo da Vinci 32, 20133 Milano, Italy

¹⁰ European XFEL, Holzkoppel 4, 22869 Schenefeld, Germany

¹¹ Department of Physics, Lund University, PO Box 118, SE-221 00 Lund, Sweden

¹² ELI-ALPS, ELI-Hu Kft., Dugonics tér 13, H-6720 Szeged, Hungary

¹³ Institute of Multidisciplinary Research for Advanced Materials, Tohoku University, Sendai 980-8577, Japan

¹⁴ Department of Physics and Astronomy, Louisiana State University, Baton Rouge, Louisiana 70803-4001, United States of America

¹⁵ Skobel'syn Institute of Nuclear Physics, Lomonosov Moscow State University, Moscow 119911, Russia

* Author to whom any correspondence should be addressed.

¹⁶ Now at Deutsches Elektronen-Synchrotron DESY, Notkestrasse 85, 22607 Hamburg, Germany.

E-mail: giuseppe.sansone@physik.uni-freiburg.de

Keywords: FEL, attosecond science, atomic molecular and atomic physics

Abstract

The generation of attosecond pulse trains at free-electron lasers opens new opportunities in ultrafast science, as it gives access, for the first time, to reproducible, programmable, extreme ultraviolet (XUV) waveforms with high intensity. In this work, we present a detailed analysis of the theoretical model underlying the temporal characterization of the attosecond pulse trains recently generated at the free-electron laser FERMI. In particular, the validity of the approximations used for the correlated analysis of the photoelectron spectra generated in the two-color photoionization experiments are thoroughly discussed. The ranges of validity of the assumptions, in connection with the main experimental parameters, are derived.

1. Introduction

Attosecond pulses of light and electrons allow one to investigate the fastest events occurring outside the nucleus [1]. In particular, attosecond pulse trains and isolated attosecond pulses enable time-resolved investigations of electronic processes occurring in atoms, molecules and surfaces by using an extreme ultraviolet (XUV) pump—near infrared (NIR) probe approach [2]. The implementation of XUV pump—XUV probe time-resolved schemes in the attosecond domain has already been demonstrated in a few experimental studies [3, 4], but its general use still remains a formidable challenge, due to the intrinsically low conversion efficiency of the high-order harmonic generation (HHG) process [5].

XUV and x-ray pulses delivered by free electron lasers (FELs) present complementary characteristics to HHG-based sources, with energies per pulse ranging from a few hundreds of μJ to a few mJ and pulse

durations typically in the femtosecond time domain. For pump–probe experiments, a main limitation of FEL-based XUV/x-ray sources is the synchronization with an external laser. Timing-jitter values depend on the specific facility, but they usually range from a few tens [6] to a few femtoseconds [7].

Several approaches have been advanced for the generation of attosecond pulses using FELs [8–10]. Recently, the generation of isolated attosecond pulses in the soft and hard x-ray spectral range was demonstrated [11, 12]. The generation scheme is based on the confinement of the lasing part of the electron bunch [13]. Due to the stochastic nature of the self-amplified spontaneous emission process, the characteristics of these pulses (spectrum, temporal structure and duration) change on a shot-to-shot basis [14], calling for a single-shot technique for their temporal characterization [15].

At the seeded FEL FERMI [16], the generation of two phase-locked harmonics was demonstrated in 2016 [17], allowing the coherent control of electronic processes by mixing XUV harmonics [18–20] and giving access to the temporal characterization of the relative phase of two XUV harmonics [21]. Multi-color phase-coherent harmonics (three and four harmonics) were also demonstrated at FERMI [22]; in this experiment, the temporal structure of the harmonic spectrum consisted of a sequence of attosecond pulses, whose temporal structure could be finely controlled by changing the relative amplitudes and phases between the harmonics. The temporal characterization was based on a cross-correlation measurement of the photoelectron spectra generated by single XUV-photon absorption and multiple-NIR photon absorption and emission. In the presence of a NIR field, the outgoing photoelectron wave packet, released by absorption of a single XUV photon, can exchange (absorb or emit) additional NIR photons. The interaction with the NIR field leads to the formation of additional lines in the photoelectron spectra, intermediate between the main lines, usually denoted as sidebands. This technique is widely used in attosecond metrology with HHG-sources for the temporal characterization of attosecond pulse trains. In this approach, usually denoted as reconstruction of attosecond bursts by beating of two-photon transitions (RABBITT) [23], the relative phase between the odd harmonics of the fundamental frequency ω_{NIR} is characterized by measuring the variations of the sideband intensities as a function of the relative delay τ between the XUV and NIR fields. The intensities oscillate with period $T = \pi/\omega_{\text{NIR}}$ and control of the relative delay well below the period of the optical cycle T is required for the observation of the oscillations. This approach cannot be employed at FELs, due to the timing jitter between the XUV waveform and the NIR field [7]. This problem was overcome by the correlation analysis of the sidebands of different energies of the single-shot photoelectron spectra. In particular, the shape of the correlation plots revealed the relative timing between the harmonics, thus giving access to the relative phase of the harmonics and allowing the reconstruction of the attosecond pulses.

In reference [22], the experimental photoelectron spectra were analyzed using a model based on the strong-field approximation (SFA). Within this framework, a few assumptions must be fulfilled to derive the form of the correlation plots. These assumptions depend on the NIR field intensity and on the energy of the photoelectrons. A detailed analysis of these assumptions is required to estimate the range of validity of the approach.

The manuscript is organized as follows: we first present the experimental setup implemented for the generation and temporal characterization of multiple phase-coherent harmonics at FERMI. We then introduce the theoretical model used to simulate the photoelectron spectra. The approximations leading to the equations describing the shape of the correlation plots are introduced. The experimental results and in particular, the calibration procedure used and the intensity dependence of the measured correlation plots, are presented. Finally, the different approximations are introduced and their validity range is discussed.

2. Experimental setup

The experimental setup is shown in figure 1. The experiment was performed at the FEL FERMI, using a seed laser with photon energy $\hbar\omega_{\text{UV}} = 4.65$ eV, obtained as the third harmonic of a NIR laser with photon energy $\hbar\omega_{\text{NIR}} = 1.55$ eV (\hbar indicates the reduced Planck constant). The six undulators available at FERMI were used for the generation of three or four harmonics of the fundamental seed pulse. The harmonics of the seed laser are generated using the technique of high gain harmonic generation [16]. Between each pair of consecutive undulators, a phase shifter (a magnetic chicane, which can extend the path followed by the electron bunch) was used to control the relative phases between the different harmonics [17, 22], by delaying the electron bunch with respect to the radiation emitted in the upstream undulators. The generated harmonics were focused in the interaction volume by a Kirkpatrick–Baez (KB) mirror setup. The NIR pulse was collinearly recombined with the XUV radiation using a drilled mirror placed between the KB mirrors and the interaction point. Both pulses were linearly polarized with polarization direction along the spectrometer axis. A delay jitter τ of about ± 3 fs was estimated between the arrival times of the two pulses at the gas target [7]. Single-shot photoelectron spectra in neon were acquired using a magnetic bottle

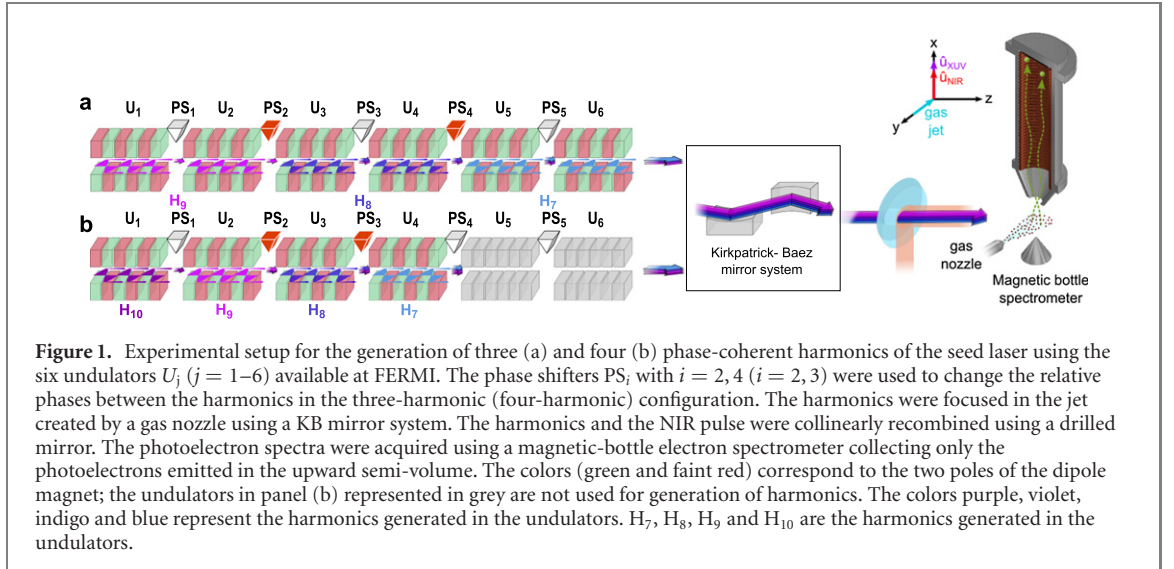


Figure 1. Experimental setup for the generation of three (a) and four (b) phase-coherent harmonics of the seed laser using the six undulators U_j ($j = 1-6$) available at FERMI. The phase shifters PS_i with $i = 2, 4$ ($i = 2, 3$) were used to change the relative phases between the harmonics in the three-harmonic (four-harmonic) configuration. The harmonics were focused in the jet created by a gas nozzle using a KB mirror system. The harmonics and the NIR pulse were collinearly recombined using a drilled mirror. The photoelectron spectra were acquired using a magnetic-bottle electron spectrometer collecting only the photoelectrons emitted in the upward semi-volume. The colors (green and faint red) correspond to the two poles of the dipole magnet; the undulators in panel (b) represented in grey are not used for generation of harmonics. The colors purple, violet, indigo and blue represent the harmonics generated in the undulators. H_7, H_8, H_9 and H_{10} are the harmonics generated in the undulators.

Table 1. Photon energies ($\hbar\omega_q$) and amplitudes (F_q) of the harmonic q for the three- (a) and four-harmonic cases (b). The amplitudes of the harmonics were rescaled to the area of the peak corresponding to the 8th harmonic. The error bars for the amplitudes were estimated from the standard deviation of the single shot harmonic intensities. The error bars for the photon energies were estimated as the fluctuations of the order of 10^{-4} of the central frequency.

	$\hbar\omega_{10}$ (eV)	$\hbar\omega_9$ (eV)	$\hbar\omega_8$ (eV)	$\hbar\omega_7$ (eV)
(a)	—	42.27 ± 0.04	37.57 ± 0.04	32.88 ± 0.03
(b)	46.96 ± 0.05	42.27 ± 0.04	37.57 ± 0.04	32.88 ± 0.03
	F_{10} (arb. u.)	F_9 (arb. u.)	F_8 (arb. u.)	F_7 (arb. u.)
(a)	—	0.95 ± 0.06	1.00 ± 0.03	0.89 ± 0.06
(b)	0.59 ± 0.07	0.76 ± 0.06	1.00 ± 0.05	1.03 ± 0.05

electron spectrometer optimised to collect only the photoelectrons emitted towards the electron detector. Typically ~ 5000 photoelectrons per laser shot were produced. For each setting of the phase shifter delays, usually 10 000–12 000 shots were acquired at 50 Hz. The intensity of the NIR pulses in the interaction region was changed by means of a half-wave plate and a polarizer placed before the recombination mirror (not shown).

For the three and four harmonic configurations, the harmonics were generated by three pairs of consecutive undulators (figure 1(a)), and four single undulators (figure 1(b)), respectively. In both the configurations, higher harmonics were generated by the first undulators and the later ones were used to generate the lower harmonics. The relative phase between the harmonics was modified using the phase shifters PS_2 and PS_4 for the three harmonic case, and the phase shifters PS_2 and PS_3 for the four harmonic case (shown in red in figure 1). The intensity of the single harmonics changed on a shot-to-shot basis by about 5%. The typical parameters of the XUV harmonics are reported in table 1. The intensity of the NIR was estimated to be $I_{\text{NIR}} = 10^{12} \text{ W cm}^{-2}$.

3. Theory

3.1. Definitions

We simulated the photoelectron spectra generated by the two-color photoionization using the following expression for the electric fields:

$$\begin{aligned}
 \mathbf{E}_{\text{XUV}}(t) &= \sum_{q=q_{\min}}^{q_{\max}} \frac{1}{2} [\tilde{E}_q(t) + \tilde{E}_q^*(t)] \mathbf{u}_{\text{XUV}} \\
 &= \sum_{q=q_{\min}}^{q_{\max}} \frac{1}{2} [F_q f(t) \exp(iq\omega_{\text{UV}}t + i\varphi_q) + \text{c.c.}] \mathbf{u}_{\text{XUV}}, \\
 \mathbf{E}_{\text{NIR}}(t, \tau) &= F_{\text{NIR}} f_{\text{NIR}}(t - \tau) \sin[\omega_{\text{NIR}}(t - \tau)] \mathbf{u}_{\text{NIR}},
 \end{aligned} \tag{1}$$

where q is the harmonic order, ω_{UV} is the central frequency of the FEL seed laser, τ is the delay between XUV and NIR, F_q and φ_q are the amplitude and phase of the q th harmonic, and F_{NIR} and $\omega_{NIR} = \omega_{UV}/3$ are the amplitude and central frequency of the NIR pulse, respectively. $\tilde{E}_q(t)$ indicates the complex form of the electric field of the q th harmonic, and q_{min} and q_{max} indicate the minimum and maximum harmonic order of the comb, \mathbf{u}_{XUV} and \mathbf{u}_{NIR} are the polarization vectors of the XUV and NIR pulses respectively. Both the XUV and NIR pulses are linearly polarized along the axis of the magnetic bottle electron spectrometer (see figure 1). In the following we will consider two cases: $(q_{min}, q_{max}) = (7, 9)$ (three-harmonic case) and $(q_{min}, q_{max}) = (7, 10)$ (four-harmonic case). We assume a Gaussian temporal envelope for each harmonic ($f(t)$) and for the NIR pulse ($f_{NIR}(t)$) with full-width at half maximum durations $FWHM_{XUV} = 50$ fs and $FWHM_{NIR} = 60$ fs, respectively. The experimental values of the duration of the different harmonics are presented in reference [24]. They show small differences for similar duration of the seed pulse. For this reason and for the sake of simplicity, we assumed in our model that all harmonics are characterized by the same pulse duration. The intensity envelope of the attosecond pulse train can be written as:

$$I(t) \propto \frac{1}{2} \left| \sum_{q=q_{min}}^{q_{max}} \tilde{E}_q(t) \right|^2 = \frac{1}{2} \left| \sum_{q=q_{min}}^{q_{max}} F_q f(t) \exp(iq\omega_{UV}t + i\varphi_q) \right|^2, \quad (2)$$

and it can be expressed in terms of the phase [22]:

$$\eta = \frac{\varphi_{q_{max}} - \varphi_{q_{min}}}{q_{max} - q_{min}}, \quad (3)$$

and of the phase differences $\Delta\varphi_{q-1,q,q+1}$:

$$\Delta\varphi_{q-1,q,q+1} = (\varphi_{q+1} - \varphi_q) - (\varphi_q - \varphi_{q-1}) = \varphi_{q+1} + \varphi_{q-1} - 2\varphi_q. \quad (4)$$

The phase η is proportional to the overall group-delay (GD) of the harmonic spectrum:

$$GD(\omega) = \frac{d\varphi(\omega)}{d\omega} \simeq \frac{(\varphi_{q_{max}} - \varphi_{q_{min}})}{(q_{max} - q_{min})\omega_{UV}} = \frac{\eta}{\omega_{UV}}, \quad (5)$$

where $\varphi(\omega)$ indicates the phase of the complete XUV spectrum. The group delay corresponds, in the limit of a long pulse train, to an overall delay between the periodic attosecond pulse structure and the temporal envelope of the single harmonic [22], and it does not affect significantly the intensity profile.

The phase difference $\Delta\varphi_{q-1,q,q+1}$ is proportional to the group-delay dispersion (GDD) of the harmonic spectrum, which is defined as the second derivative of the spectral phase with respect to the frequency:

$$GDD(\omega) = \frac{d^2\varphi(\omega)}{d\omega^2} \simeq \frac{(\varphi_{q+1} - \varphi_q)/\omega_{UV} - (\varphi_q - \varphi_{q-1})/\omega_{UV}}{\omega_{UV}} = \frac{\Delta\varphi_{q-1,q,q+1}}{\omega_{UV}^2}. \quad (6)$$

As we will show in the following section our experimental approach gives direct access to the GDD of the harmonic comb.

The phase of the harmonics can be controlled through phase shifters, which introduce a controllable delay τ_s between the different harmonics. In particular, in the experiment with three harmonics the phase shifters PS₂ ($j = 2$) and PS₄ ($k = 4$) were used, while for the four harmonic case the phase shifters PS₂ ($j = 2$) and PS₃ ($k = 3$) were implemented. The additional phases of the harmonics are then given by:

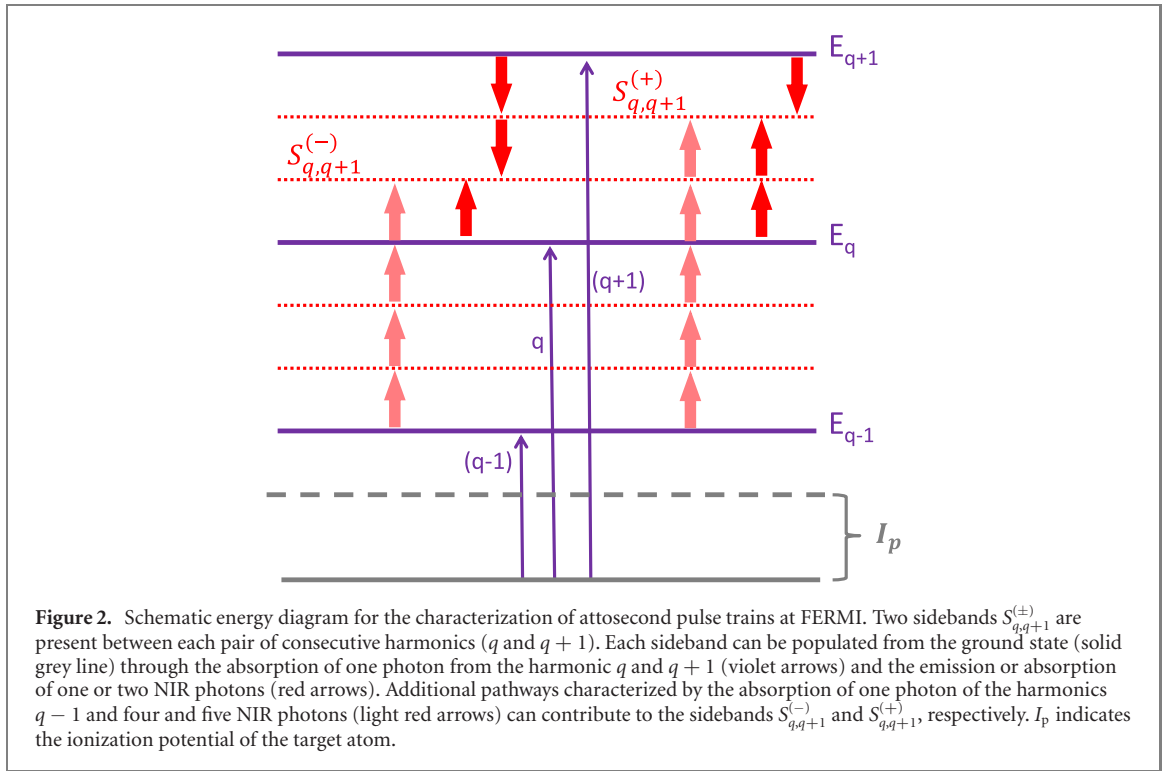
$$\begin{aligned} \varphi_{10} &= \varphi_{10}^{(0)}, & \varphi_9 &= \varphi_9^{(0)}, \\ \varphi_8 &= \varphi_8^{(0)} - 8\omega_{UV}(\tau_{sj}), & \varphi_7 &= \varphi_7^{(0)} - 7\omega_{UV}(\tau_{sj} + \tau_{sk}), \end{aligned} \quad (7)$$

where $\varphi_q^{(0)}$ indicates the initial phase of the q th harmonic. The phase differences $\Delta\varphi_{7,8,9}$ and $\Delta\varphi_{8,9,10}$ are thus expressed by the relations:

$$\Delta\varphi_{8,9,10} = \left(\varphi_{10}^{(0)} + \varphi_8^{(0)} - 2\varphi_9^{(0)} \right) - 8\omega_{UV}\tau_{sj}, \quad (8)$$

$$\Delta\varphi_{7,8,9} = \left(\varphi_9^{(0)} + \varphi_7^{(0)} - 2\varphi_8^{(0)} \right) + 9\omega_{UV}\tau_{sj} - 7\omega_{UV}\tau_{sk}. \quad (9)$$

The phase difference $\Delta\varphi_{8,9,10}$ ($\Delta\varphi_{7,8,9}$) depends only on the delay τ_{sj} (τ_{sj}, τ_{sk}).



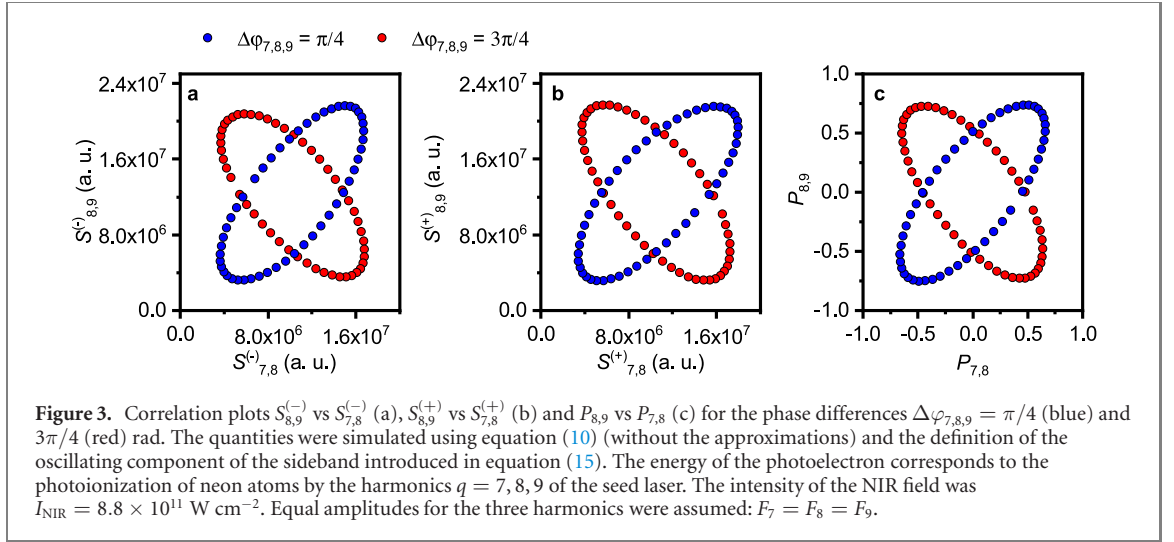
3.2. Theoretical model

The simulations of the photoelectron spectra generated by the combination of the XUV attosecond waveforms ($\mathbf{E}_{\text{XUV}}(t)$) and the NIR ($\mathbf{E}_{\text{NIR}}(t)$) pulses are based on the SFA [25]. The amplitude of the photoelectron wave packet emitted with final momentum \mathbf{p} for a delay τ between the XUV and NIR pulses, $b(\mathbf{p}, \tau)$, is given by (atomic units are used) [26–28]:

$$b(\mathbf{p}, \tau) = i \int_{-\infty}^{+\infty} dt' \mathbf{E}_{\text{XUV}}(t') \mathbf{d} [\mathbf{p} + \mathbf{A}_{\text{NIR}}(t', \tau)] \exp \left\{ -i \int_{t'}^{+\infty} dt'' \left[\frac{1}{2} (\mathbf{p} + \mathbf{A}_{\text{NIR}}(t'', \tau))^2 \right] + i I_p t' \right\}, \quad (10)$$

where $\mathbf{A}_{\text{NIR}}(t)$ is the vector potential of the NIR pulse, t' the ionisation instant, I_p the ionisation potential of the atom, and $\mathbf{d} [\mathbf{p} + \mathbf{A}_{\text{NIR}}(t', \tau)]$ is the matrix element of the dipole operator describing the transition from the ground state to the continuum state with momentum $\mathbf{p} + \mathbf{A}_{\text{NIR}}(t', \tau)$ after the absorption of an XUV photon. Important information on the correlated variation of the sidebands can be derived analytically from equation (10). For the sake of simplicity, we neglect the slow intensity variation due to the envelopes $f(t)$, $f_{\text{NIR}}(t)$ and consider a constant amplitude of the single XUV harmonic and NIR field in deriving the equations of the sideband intensities. For intensities of the NIR field less than $3 \times 10^{12} \text{ W cm}^{-2}$, we can also neglect the term proportional to A_{NIR}^2 in equation (10). We will indicate this approximation as *approximation I* (see section 5.1). We will comment on the validity of this approximation (and also on two additional ones) in section 5. Moreover, we assume that the dipole matrix element is constant over the energy range spanned by the XUV spectrum ($\mathbf{d} = \text{const.}$). The assumption of constant dipole matrix element implies that we cannot analyze the contribution of the different partial waves to the photoionization spectrum. A more detailed description involving the contribution of the different partial waves using the perturbation theory is given in the supplementary material of the earlier publication [22]. The results from the perturbation theory in the approximation of equal amplitudes of the harmonics support the simulations based on the SFA approximation, confirming that the intensities of the sidebands oscillate as a function of the phase difference between the harmonics even after integrating over the half hemisphere. We consider only electrons emitted parallel to the polarisation direction of the two fields: $\mathbf{p} \parallel \mathbf{u}_{\text{XUV,NIR}}$. These approximations allow one to identify the most relevant properties of the sidebands generated in the two-color field. The term $\mathbf{p} \cdot \mathbf{A}_{\text{NIR}}(t'', \tau)$, arising from the phase factor in equation (10), can be expanded in Bessel functions J_n using the relation:

$$e^{ix \sin \phi} = \sum_{n=-\infty}^{+\infty} J_n(x) e^{in\phi}. \quad (11)$$



Different pathways can lead to the population of the sidebands as shown in figure 2. Depending on the intensity of the NIR field, a different number of exchanged NIR photons must be considered. We first consider the case of up to two-NIR photon transitions (*approximation II*, discussed in section 5.2):

$$e^{ix \sin \phi} \approx J_{-1}(x)e^{-i\phi} + J_0(x) + J_1(x)e^{i\phi}. \quad (12)$$

The intensities of two consecutive sidebands can be then expressed as:

$$\begin{aligned} S_{q,q+1}^{(-)}(x_{q,q+1}^{(-)}) &= \frac{1}{4} [J_1^2 F_q^2 - 2J_1 J_2 F_q F_{q+1} \cos(3\omega_{\text{NIR}}\tau + \varphi_{q+1} - \varphi_q) + J_2^2 F_{q+1}^2], \\ S_{q,q+1}^{(+)}(x_{q,q+1}^{(+)}) &= \frac{1}{4} [J_2^2 F_q^2 + 2J_1 J_2 F_q F_{q+1} \cos(3\omega_{\text{NIR}}\tau + \varphi_{q+1} - \varphi_q) + J_1^2 F_{q+1}^2], \end{aligned} \quad (13)$$

where

$$\begin{aligned} x_{q,q+1}^{(-)} &= \sqrt{2[(q+1/3)\omega_{\text{UV}} - I_p]F_{\text{NIR}}/\omega_{\text{NIR}}^2}, \\ x_{q,q+1}^{(+)} &= \sqrt{2[(q+2/3)\omega_{\text{UV}} - I_p]F_{\text{NIR}}/\omega_{\text{NIR}}^2}. \end{aligned} \quad (14)$$

For the sake of simplicity, the argument $x_{q,q+1}^{(\pm)}$ for the Bessel functions has been omitted. Worthwhile to mention that integration over the entire solid angle (4π sr) of the photoelectron spectrum cancels out the sideband oscillations as a function of the relative phase of the harmonics. This is a direct consequence of the opposite symmetry of the final continuum state reached by the two different pathways leading to the same final energy. The opposite symmetry is the result of the different number of photons involved in the two pathways.

It follows from equation (13) that the correlation plots $S_{q-1,q}^{(\pm)}(x_{q-1,q}^{(\pm)})$ vs $S_{q,q+1}^{(\pm)}(x_{q,q+1}^{(\pm)})$ are described by ellipses, whose shape depends on the phase difference $\Delta\varphi_{q-1,q,q+1}$.

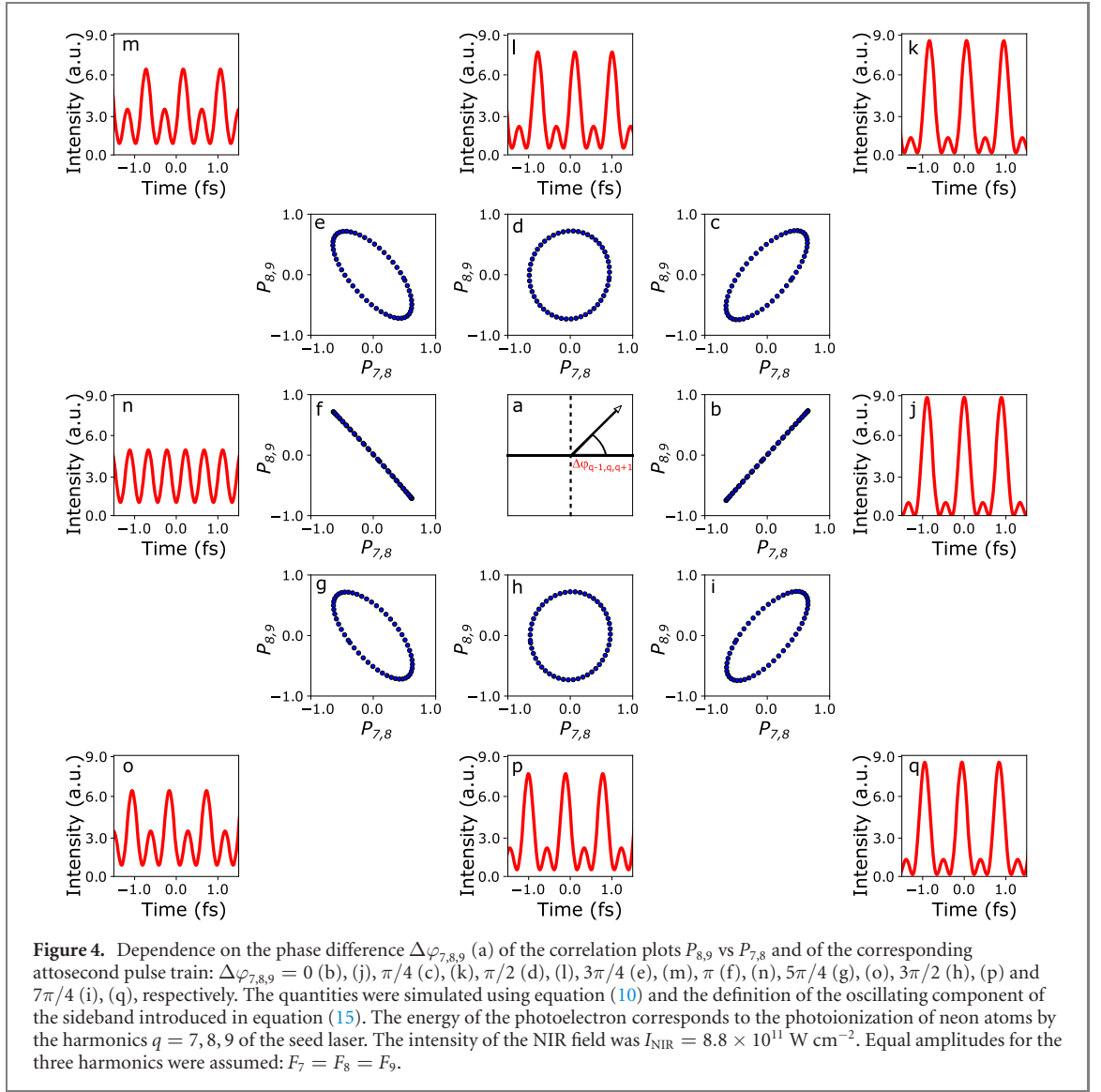
Figures 3(a) and (b) present the correlation plots $S_{8,9}^{(\pm)}$ vs $S_{7,8}^{(\pm)}$ for the phase differences $\Delta\varphi_{7,8,9} = \pi/4$ and $3\pi/4$ rad. The shape (eccentricity) of the ellipses gives direct access to the phase difference $\Delta\varphi_{7,8,9}$. For the analysis of the experimental data, however, it is more convenient to consider only the oscillating component of the sidebands, which can be extracted by using the definition:

$$P_{q,q+1} = \frac{S_{q,q+1}^{(+)} - S_{q,q+1}^{(-)}}{S_{q,q+1}^{(+)} + S_{q,q+1}^{(-)}}. \quad (15)$$

Under the approximation (see section 5.3):

$$\Delta x_{q,q+1} = \frac{1}{2} [x_{q,q+1}^{(+)} - x_{q,q+1}^{(-)}] \approx 0 \quad (\text{Approximation III}), \quad (16)$$

it follows that the oscillating component can be expressed as:



$$\begin{aligned}
 P_{q,q+1} &= \frac{J_2^2 - J_1^2}{J_2^2 + J_1^2} \frac{F_q^2 - F_{q+1}^2}{F_q^2 + F_{q+1}^2} + \frac{4J_1J_2}{J_1^2 + J_2^2} \frac{F_qF_{q+1}}{F_q^2 + F_{q+1}^2} \cos[\varphi_{q+1} - \varphi_q + 3\omega_{\text{NIR}}\tau] \\
 &= \beta_{q,q+1} + \alpha_{q,q+1} \cos \Phi,
 \end{aligned} \tag{17}$$

where:

$$\begin{aligned}
 \beta_{q,q+1} &= \frac{J_2^2 - J_1^2}{J_2^2 + J_1^2} \frac{F_q^2 - F_{q+1}^2}{F_q^2 + F_{q+1}^2}, \\
 \alpha_{q,q+1} &= \frac{4J_1J_2}{J_1^2 + J_2^2} \frac{F_qF_{q+1}}{F_q^2 + F_{q+1}^2}, \\
 \Phi &= \varphi_{q+1} - \varphi_q + 3\omega_{\text{NIR}}\tau.
 \end{aligned} \tag{18}$$

For equal amplitudes of the harmonics ($F_q = F_{q+1}$) it follows that:

$$\beta_{q,q+1} = 0, \quad \alpha_{q,q+1} = \frac{2J_1J_2}{J_1^2 + J_2^2}. \tag{19}$$

The correlated plots of the oscillating components $P_{q,q+1}$ and $P_{q-1,q}$ are also described by ellipses according to the equation:

$$\begin{aligned}
 \frac{[P_{q-1,q} - \beta_{q-1,q}]^2}{\alpha_{q-1,q}^2} + \frac{[P_{q,q+1} - \beta_{q,q+1}]^2}{\alpha_{q,q+1}^2} - 2 \frac{[P_{q-1,q} - \beta_{q-1,q}][P_{q,q+1} - \beta_{q,q+1}]}{\alpha_{q-1,q}\alpha_{q,q+1}} \cos \Delta\varphi_{q-1,q,q+1} \\
 = \sin^2 \Delta\varphi_{q-1,q,q+1}.
 \end{aligned} \tag{20}$$

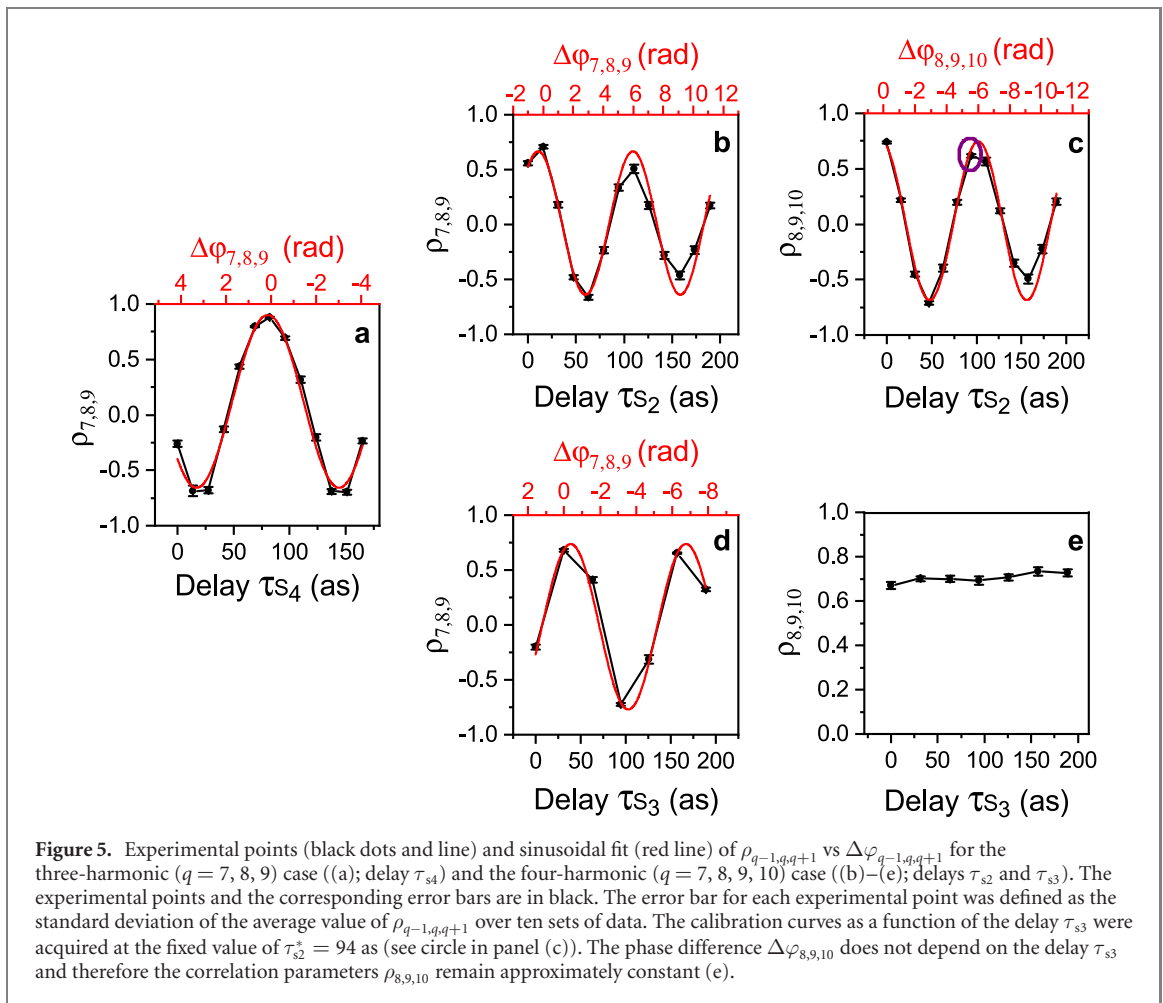


Figure 3(c) presents the correlation plot $P_{8,9}$ vs $P_{7,8}$, without any approximations apart from the assumption of equal amplitudes of the harmonics. The correlation plots based on the sideband intensities $S_{q,q+1}^{(\pm)}$ (figures 3(a) and (b)) or on the oscillating component $P_{q,q+1}$ follow similar curves and they are described, within our approximation, by similar equations. Therefore the phase information between the harmonics can be extracted, in principle, from each of the three different correlation plots. However we will show, in the analysis of the experimental data that the correlation plots based on the oscillating component are less sensitive to the single-shot fluctuations of the single harmonics and they allow a reliable extraction of the phase information.

The complete evolution of the correlation plots for the oscillating component of the sideband, with the associated intensity profile of the attosecond pulse train is shown for the three-harmonic case in figure 4. It can be observed that similar correlation plots (for example figures 4(c) and (i); 4(d) and (h) and 4(e) and (g)) correspond to different phases $\Delta\varphi_{7,8,9}$ and, therefore, to different reconstructed electric fields. Generally, the phase differences $\Delta\varphi_{q-1,q,q+1} = \varphi_0$ and $\Delta\varphi_{q-1,q,q+1} = 2\pi - \varphi_0$ are related to the same correlation plot as shown by equation (20). This ambiguity can be resolved in the experiment by changing the relative phases between the harmonics by a known amount. In particular, as the sign of the delays (and therefore of the phases) introduced on the harmonics are known, it is possible to assign unequivocally a phase difference to each correlation plot.

3.3. Correlation parameter

In the experiment, the photoelectron spectra were measured for a fixed setting of the phase shifters. We indicate with $S_{q,q+1}^{(\pm)}(i)$ ($i = 1, 2, 3, \dots, N$) the intensity of the sideband $S_{q,q+1}^{(\pm)}$ for the i th-FEL shot. The intensity of each sideband was obtained by numerical integration of the corresponding peak in the time-of-flight spectrum. The oscillating component of the sidebands $P_{q,q+1}$ was determined according to equation (15) after subtraction of the background.

The phase information is encoded in the shape of the ellipses. However, an elliptical fit of the correlation plots $P_{q-1,q}$ vs $P_{q,q+1}$ was problematic, due to the residual single harmonic fluctuations, which lead to scattered experimental points. In order to evaluate the changes of the shape of the correlation plots for

different phases, we used the correlation coefficient $\rho_{q-1,q,q+1}$ defined as:

$$\rho_{q-1,q,q+1} = \frac{\text{cov}(x, y)}{\sigma_x \sigma_y} = \frac{\langle xy \rangle - \langle x \rangle \langle y \rangle}{\sqrt{\langle x^2 \rangle - \langle x \rangle^2} \sqrt{\langle y^2 \rangle - \langle y \rangle^2}}, \quad (21)$$

where $x \equiv P_{q-1,q}(i)$, $y \equiv P_{q,q+1}(i)$ and

$$\langle x \rangle = \frac{\sum_{i=1}^N x(i)}{N} \quad i = 1, 2, 3, \dots, N, \quad (22)$$

where N is the total number of single-shot data. A similar definition was used for $\langle y \rangle$. Numerical simulations (see figure 4) indicate that perfect positive (negative) correlation $\rho_{q-1,q,q+1} = +1(-1)$ corresponds to the condition $\Delta\varphi_{q-1,q,q+1} = 0(\pi)$ as shown in figures 4(b) and (f). Correlation coefficient $\rho_{q-1,q,q+1} = 0$ indicates that $\Delta\varphi_{q-1,q,q+1} = \pi/2 (3\pi/2)$ as shown in figures 4(d) and (h). In general, as already observed, each value of the correlation coefficient corresponds to two different phase differences $\Delta\varphi_{q-1,q,q+1} = \varphi_0$ and $\Delta\varphi_{q-1,q,q+1} = 2\pi - \varphi_0$ (or $\Delta\varphi_{q-1,q,q+1} = -\varphi_0$) (see equation (20)).

4. Experimental results and comparison with theoretical simulations

4.1. Phase calibration procedure

4.1.1. Three-harmonic case

In the case of three harmonics, the temporal structure of the attosecond pulse train depends only on the phase difference $\Delta\varphi_{7,8,9}$. In order to assign a phase value to each position of the phase shifter, a scan of the delay introduced by one phase shifter is acquired. In figure 5(a) we report the variation of the correlation parameter $\rho_{7,8,9}$ as a function of the delay τ_{s4} introduced by the phase shifter PS_4 . The phase difference $\Delta\varphi_{7,8,9}$ changes according to equation (9). The experimental points can be fitted by a sinusoidal function and the maxima of the fit are assigned to phase difference $\Delta\varphi_{7,8,9} = 2m\pi$. Using this approach each delay introduced by the phase shifter is unequivocally associated with a phase difference $\Delta\varphi_{7,8,9}$.

4.1.2. Four-harmonic case

In the four-harmonic case, the intensity profile depends on two phase differences $\Delta\varphi_{7,8,9}$ and $\Delta\varphi_{8,9,10}$. As a consequence, at least two different phase shifters can be used to control the relative phases: for example PS_2 (delay τ_{s2}) and PS_3 (delay τ_{s3}) for $\Delta\varphi_{7,8,9}$, and PS_1 (delay τ_{s1}) and PS_2 (delay τ_{s2}) for $\Delta\varphi_{8,9,10}$. In figures 5(b)–(e) we report the calibration curves for the phase shifters PS_2 and PS_3 . When changing the delay introduced by PS_2 , the phase difference $\Delta\varphi_{8,9,10}$ changes according to equation (8). Similar to the three-harmonic case, the maxima are assigned to phase differences $\Delta\varphi_{8,9,10} = 2m\pi$. The changes in τ_{s2} affect also the phase difference $\Delta\varphi_{7,8,9}$ according to equation (9).

For the calibration of the delay τ_{s3} , a fixed value of τ_{s2} was used ($\tau_{s2}^* = 94$ as) and the delay introduced by PS_3 was changed. The point corresponding to the value of τ_{s2}^* is indicated by a circle in figure 5(c). Equation (9) again allows us to assign to each delay τ_{s3} a value for the phase difference $\Delta\varphi_{7,8,9}$ imposing the condition that the maxima correspond to $\Delta\varphi_{7,8,9} = 2n\pi$.

Using this procedure we can assign the phase differences $\varphi_{7,8,9}$ and $\varphi_{8,9,10}$ for each combination of delays introduced by the phase shifters PS_2 and PS_3 . A similar procedure can be followed to calibrate the phase differences for more than four harmonics.

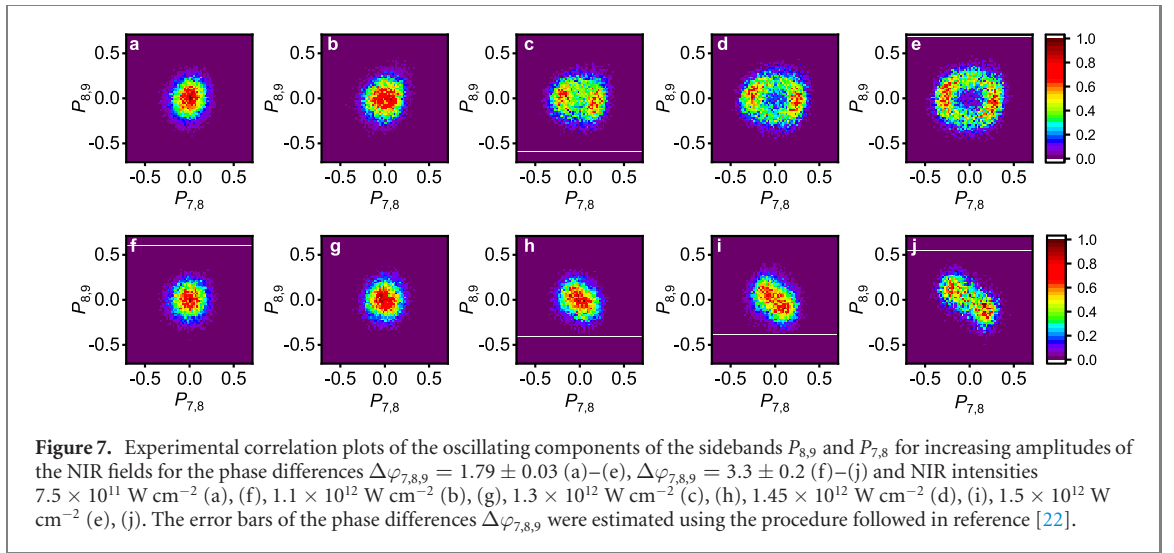
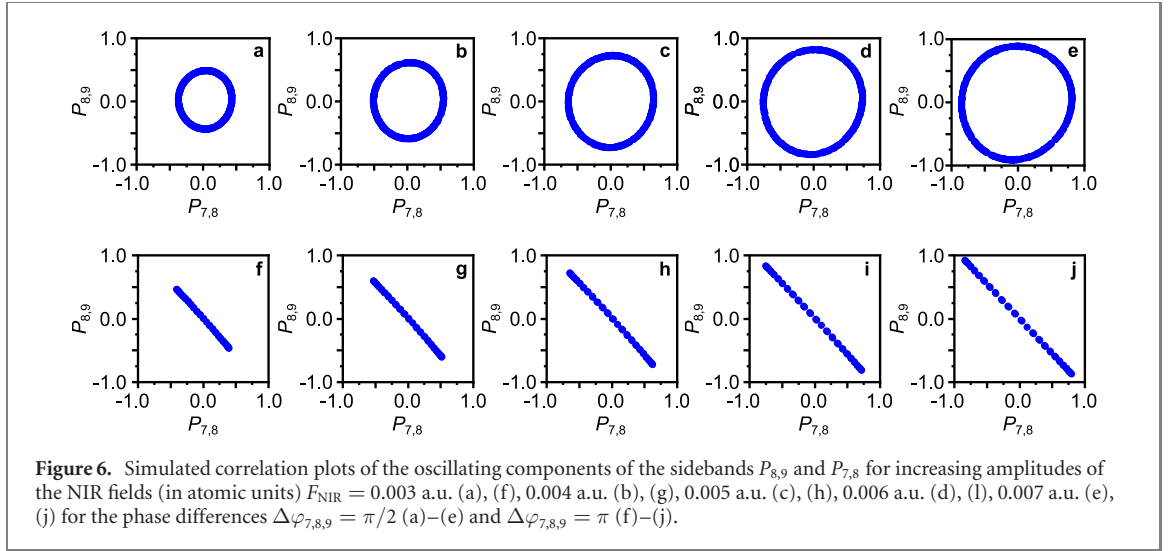
4.2. NIR-intensity dependence of the elliptical correlation plots

The NIR intensity plays an important role for the observation and the correct reconstruction of the phase differences $\Delta\varphi_{q-1,q,q+1}$. On one hand the NIR field should be sufficiently intense to overcome the single-shot fluctuations of the single harmonics, which cause the scattering of the experimental points in the correlation plots, thus preventing the observation of phase-dependent correlation plots for very low NIR intensity. On the other hand the NIR field should not be so intense as to introduce $n \geq 4$ transitions, which would invalidate approximation II (see equation (12)), thus affecting the phase reconstruction. These two conditions set a NIR intensity interval for the experiment.

The area of an ellipse is given by $S = \pi ab$, where a and b indicate the minor and major axis of the ellipse. For the correlation plots, we consider the approximation $\alpha_{q-1,q} \simeq \alpha_{q,q+1} = \alpha$ and the area of the plots is then given by:

$$A = \pi \alpha^2 |\sin \Delta\varphi_{q-1,q,q+1}|. \quad (23)$$

The area of the ellipse depends on the phase $\Delta\varphi_{q-1,q,q+1}$ between the harmonics and it reduces to zero in the case of perfect constructive ($\Delta\varphi_{q-1,q,q+1} = 0$) or destructive ($\Delta\varphi_{q-1,q,q+1} = -\pi$) synchronization.



Assuming that the harmonics also present equal amplitudes and neglecting the variation of the photoelectron energies for two consecutive sidebands, α is given by equation (19). The factor α depends on the intensity of the NIR field and on the photoelectron energy. In figures 6(a)–(e) and (f)–(j) we report the simulated correlation plots corresponding to $\Delta\varphi_{q-1,q,q+1} = 0$ and $\Delta\varphi_{q-1,q,q+1} = \pi/2$ for increasing NIR intensities (see caption), respectively.

The expected increase in the area of the ellipse with intensity was observed in the experiment as shown in figures 7(a)–(e) and (f)–(j), which reports the evolution of the correlation plots for five different intensities of the NIR field with a maximum NIR intensity of $I_{\text{NIR}} = 1.5 \times 10^{12} \text{ W cm}^{-2}$ (figures 7(e) and (j)). It can be observed that only from a NIR intensity $I_{\text{NIR}} = 1.3 \times 10^{12} \text{ W cm}^{-2}$ (figure 7(c)) the characteristic elliptical shape induced by the different $\Delta\varphi_{7,8,9}$ can be distinguished.

4.3. Correlation plots of the sideband intensities $S_{q-1,q}^{(\pm)} - S_{q,q+1}^{(\pm)}$ vs correlation plots of the oscillating component of the sideband $P_{q-1,q} - P_{q,q+1}$

We now consider the effect of single-shot fluctuations of the individual harmonics on the correlations plots. We will show that plots based on the oscillating components of the sidebands are less sensitive to harmonic intensity fluctuations than those based on the sidebands themselves, thus enabling a more reliable reconstruction of the phase differences $\Delta\varphi_{q-1,q,q+1}$. The sideband intensities $S_{q,q+1}^{(\pm)}$ for small variations of the amplitude of the single harmonic $\Delta F_{q-1}, \Delta F_q, \Delta F_{q+1}$ are described by the relations:

$$S_{q,q+1}^{(-)}[F_q + \Delta F_q, F_{q+1} + \Delta F_{q+1}] = S_{q,q+1}^{(-)}[F_q, F_{q+1}] + \frac{1}{2}F_q\Delta F_q J_1^2 + \frac{1}{2}F_{q+1}\Delta F_{q+1} J_2^2 - \frac{1}{2}(F_{q+1}\Delta F_q + F_q\Delta F_{q+1})J_1 J_2 \cos \Phi, \quad (24)$$

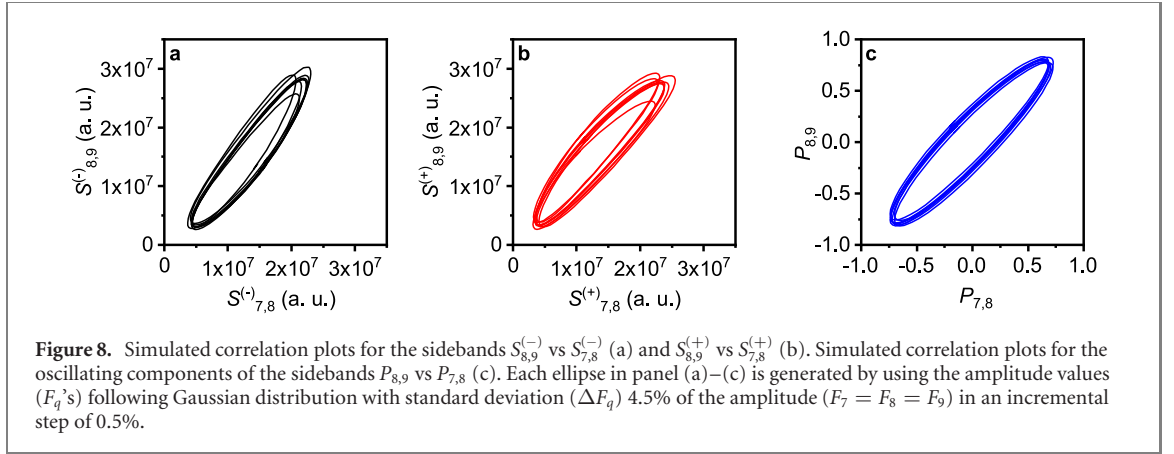


Figure 8. Simulated correlation plots for the sidebands $S_{8,9}^{(-)}$ vs $S_{7,8}^{(-)}$ (a) and $S_{8,9}^{(+)}$ vs $S_{7,8}^{(+)}$ (b). Simulated correlation plots for the oscillating components of the sidebands $P_{8,9}$ vs $P_{7,8}$ (c). Each ellipse in panel (a)–(c) is generated by using the amplitude values (F_q 's) following Gaussian distribution with standard deviation (ΔF_q) 4.5% of the amplitude ($F_7 = F_8 = F_9$) in an incremental step of 0.5%.

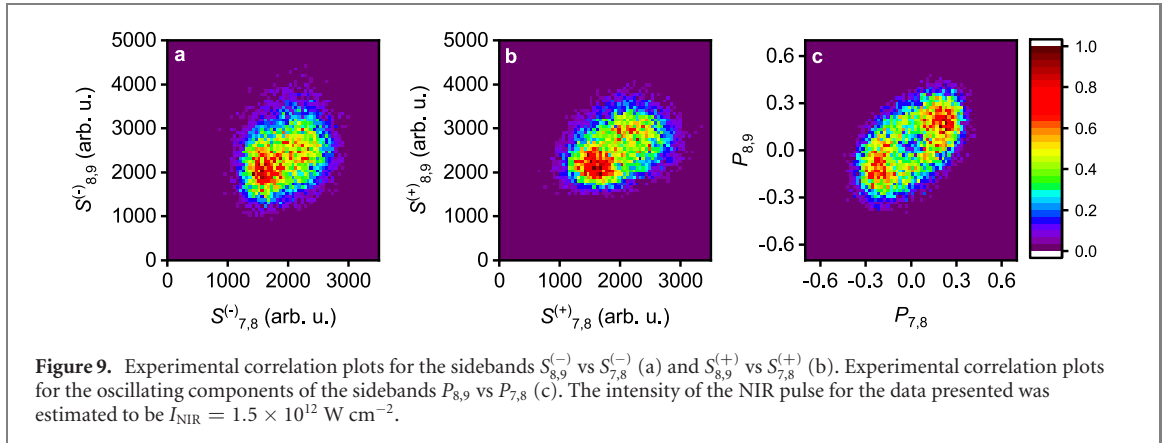


Figure 9. Experimental correlation plots for the sidebands $S_{8,9}^{(-)}$ vs $S_{7,8}^{(-)}$ (a) and $S_{8,9}^{(+)}$ vs $S_{7,8}^{(+)}$ (b). Experimental correlation plots for the oscillating components of the sidebands $P_{8,9}$ vs $P_{7,8}$ (c). The intensity of the NIR pulse for the data presented was estimated to be $I_{\text{NIR}} = 1.5 \times 10^{12} \text{ W cm}^{-2}$.

$$S_{q,q+1}^{(+)}[F_q + \Delta F_q, F_{q+1} + \Delta F_{q+1}] = S_{q,q+1}^{(+)}[F_q, F_{q+1}] + \frac{1}{2}F_q\Delta F_q J_2^2 + \frac{1}{2}F_{q+1}\Delta F_{q+1} J_1^2 + \frac{1}{2}(F_{q+1}\Delta F_q + F_q\Delta F_{q+1})J_1 J_2 \cos \Phi, \quad (25)$$

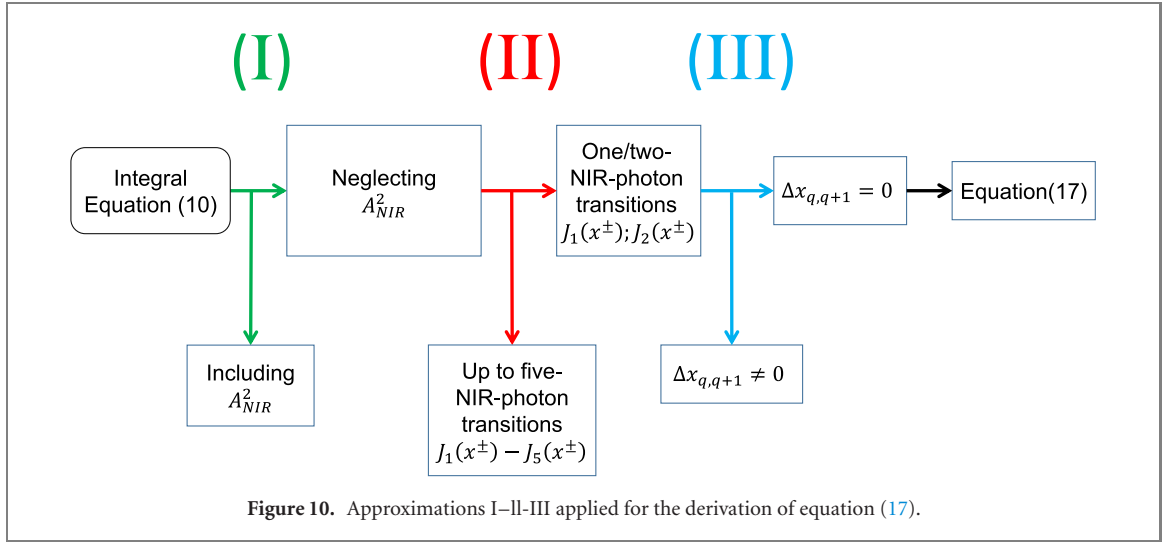
where Φ is defined by equation (18). The effect of a change of the harmonic amplitudes ΔF_q and ΔF_{q+1} on the sideband intensities depends on the phase Φ . This effect is visible in figure 8, which displays the simulated correlation plots based on the sidebands $S_{8,9}^{(-)} - S_{7,8}^{(-)}$ (a) and $S_{8,9}^{(+)} - S_{7,8}^{(+)}$ (b) for $\Delta\varphi_{7,8,9} = \pi/8$ and different variations $\Delta F_7, \Delta F_8, \Delta F_9$ (see caption) of the single harmonic amplitudes, according to equations (24) and (25). It is clear that the variations are larger for large values of the sideband signal, while the fluctuations are reduced for small sideband intensities (closer to the origin). Using the oscillating component of the sideband $P_{q,q+1}$ and expansion similar to that of equations (24) and (25), we obtain from equation (17):

$$P_{q,q+1}[F_q + \Delta F_q, F_{q+1} + \Delta F_{q+1}] = P_{q,q+1}[F_q, F_{q+1}] + 4 \frac{J_2^2 - J_1^2}{J_2^2 + J_1^2} \left(\frac{F_q F_{q+1}}{F_q^2 + F_{q+1}^2} \right)^2 \left[\frac{\Delta F_q}{F_q} - \frac{\Delta F_{q+1}}{F_{q+1}} \right] + 4 \frac{J_1 J_2}{J_1^2 + J_2^2} \cos \Phi \frac{F_q F_{q+1} (F_q^2 - F_{q+1}^2)}{(F_q^2 + F_{q+1}^2)^2} \left[\frac{\Delta F_q}{F_q} - \frac{\Delta F_{q+1}}{F_{q+1}} \right]. \quad (26)$$

In particular in the case $F_q = F_{q+1}$ the expression reduces to:

$$P_{q,q+1}[F_q + \Delta F_q, F_{q+1} + \Delta F_{q+1}] = \alpha_{q,q+1} \cos(\Phi) + \frac{J_2^2 - J_1^2}{J_2^2 + J_1^2} \frac{[\Delta F_q - \Delta F_{q+1}]}{F_q}. \quad (27)$$

Under these conditions a variation of the harmonic intensity leads only to a shift of the value of the parameter $P_{q-1,q}$, independent of the phase Φ , as shown in figure 8(c). Moreover, in the case of the oscillating component $P_{q,q+1}$ the effect cancels out for equal relative variations of the harmonic amplitudes.



The different qualitative dependence of the correlation plots on the harmonic amplitude fluctuations can be observed in the experimental data presented in figure 9. For the correlation plots based on the sideband intensities figures 9(a) and (b), the elliptical shape is barely visible and the plots present maxima closer to the origin, where the spread of the single-shot experimental points is smaller. In figure 9(c), the elliptical and symmetrical shape is clearly visible and also the central minimum appears. As a result, the analysis of the experimental data using the oscillating component of the sideband allows one to reduce the effect of the harmonic intensity fluctuations.

5. Analysis of the approximations

According to equations (17) and (20), the correlation plots are described by ellipses and information on the phase difference $\Delta\varphi_{q-1,q,q+1}$ is encoded in the shape of the ellipse. The derivation of equation (17) is based on a few assumptions (as schematically shown in figure 10) that need to be analyzed to evaluate the validity of the approach. The different assumptions are shown schematically in figure 10. In the following section, we will analyze the different approximations, using the strong-field-model, deriving, in particular, the maximum NIR intensities for which the approximations are valid.

5.1. Approximation I: role of $A_{\text{NIR}}^2 \approx 0$

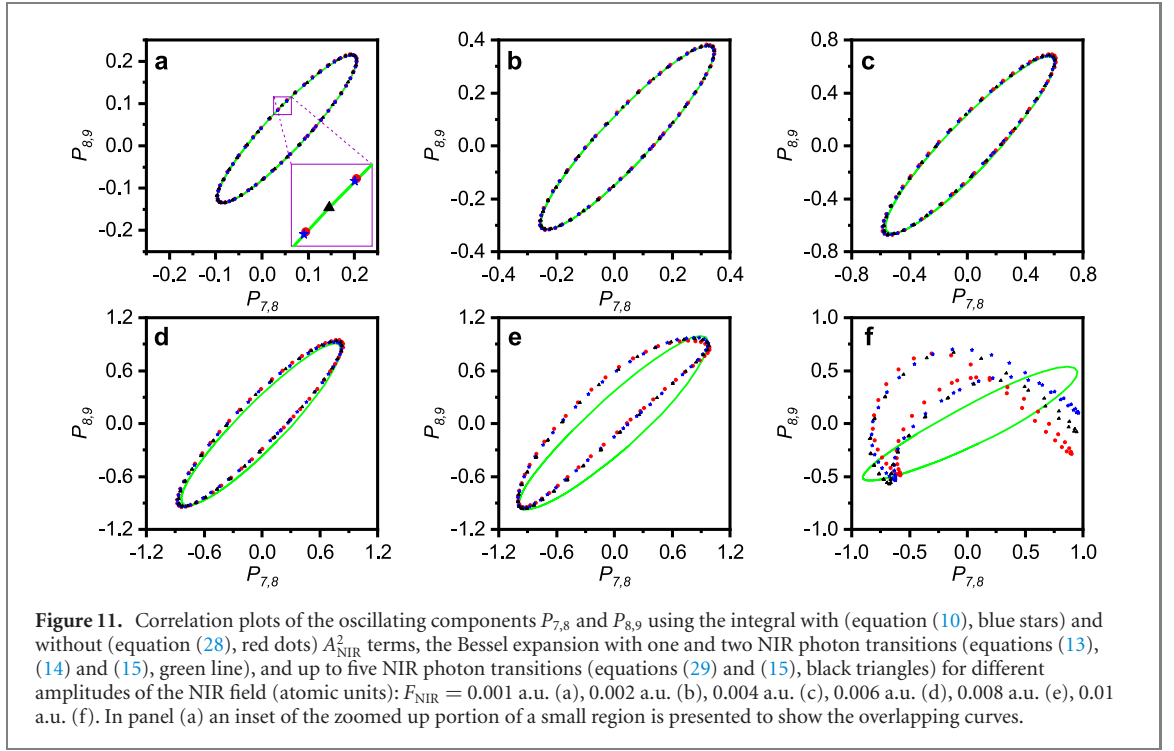
We consider the first approximation by neglecting the term $A_{\text{NIR}}^2(t'', \tau)$ in the evaluation of the integral equation (10), which leads to the expression:

$$b(\mathbf{p}, \tau) \simeq i \int_{-\infty}^{+\infty} dt' E_{\text{XUV}}(t') \exp \left\{ -i \int_{t'}^{+\infty} dt'' \left[\frac{1}{2} p^2 + \mathbf{p} \cdot \mathbf{A}_{\text{NIR}}(t'', \tau) \right] + i I_{\text{p}} t' \right\}, \quad (28)$$

where we also assumed that the dipole matrix element $\mathbf{d}[\mathbf{p} + \mathbf{A}_{\text{NIR}}(t', \tau)]$ is constant. The results are shown in figure 11 for increasing NIR fields. We can observe that at low intensity of the NIR the agreement between the two curves with (blue stars) and without (red dots) the term A_{NIR}^2 is excellent. Also for intensities higher than $F_{\text{NIR}} = 0.01$ a.u. the shape of the correlated sideband parameter is very similar, even though there is a small offset, which does not appreciably affect the evaluation of the correlation coefficient defined in equation (21). The conclusion is that, at least up to $F_{\text{NIR}} \approx 0.01$ a.u., the term A_{NIR}^2 can be safely neglected.

5.2. Approximation II: multi-NIR photon transitions

The integral of equation (28) can be evaluated using a Bessel expansion of the exponential term containing $\mathbf{p} \cdot \mathbf{A}_{\text{NIR}}(t'', \tau)$. For low NIR intensities, the assumption that only one and two-NIR-photon transitions play a role in the appearance of the sidebands is well justified. For higher intensities, however, also higher-order NIR transitions start to play a role. We analyze the contribution of these multi-NIR photon ($n > 2$)



transitions, by comparing the expansions:

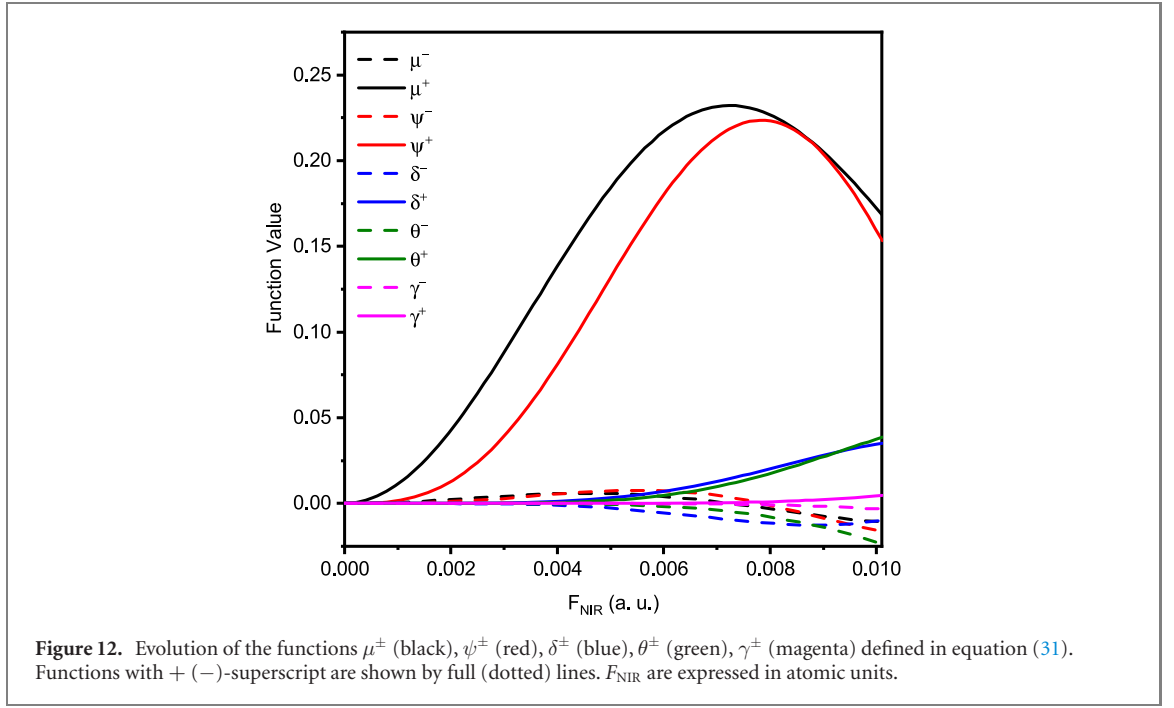
$$\begin{aligned}
 S_{q,q+1}^{(+)}(x_{q,q+1}^{(+)}) &= \frac{1}{4} \{ J_5^2 F_{q-1}^2 + J_2^2 F_q^2 + J_1^2 F_{q+1}^2 - 2F_{q-1} F_q J_2 J_5 \cos[3\omega_{\text{NIR}}\tau + \varphi_q - \varphi_{q-1}] \\
 &\quad - 2F_{q-1} F_{q+1} J_5 J_1 \cos[6\omega_{\text{NIR}}\tau + \varphi_{q+1} - \varphi_{q-1}] \\
 &\quad + 2F_q F_{q+1} J_2 J_1 \cos[3\omega_{\text{NIR}} + \varphi_{q+1} - \varphi_q] \}, \quad (29)
 \end{aligned}$$

$$\begin{aligned}
 S_{q,q+1}^{(-)}(x_{q,q+1}^{(-)}) &= \frac{1}{4} [J_4^2 F_{q-1}^2 + J_1^2 F_q^2 + J_2^2 F_{q+1}^2 - 2F_{q-1} F_q J_4 J_1 \cos[3\omega_{\text{NIR}}\tau + \varphi_q - \varphi_{q-1}] \\
 &\quad + 2F_{q-1} F_{q+1} J_4 J_2 \cos[6\omega_{\text{NIR}}\tau + \varphi_{q+1} - \varphi_{q-1}] \\
 &\quad - 2F_q F_{q+1} J_1 J_2 \cos[3\omega_{\text{NIR}} + \varphi_{q+1} - \varphi_q], \quad (30)
 \end{aligned}$$

which were obtained by considering terms up to the fifth order ($n = 5$) in the expansion of equation (11). Figure 11 presents the comparison between the correlation plots of the oscillating components of the sidebands determined using the two Bessel-based expansions with terms up to the second (green line) and fifth order (black triangles). It is evident that already starting from $F_{\text{NIR}} = 0.008$ a.u. the approximation with only one and two-NIR-photon transitions is poorly fulfilled and the inclusion of higher terms in the Bessel-based expansion is important in order to obtain a good approximation.

This conclusion is confirmed by analysing the contribution to the sideband intensities and to the oscillating component $P_{q,q+1}$ due to the different multiphoton terms. For this purpose we introduce the following functions:

$$\begin{aligned}
 \gamma^\pm &= \frac{1}{4} [J_5^2(x^+) \pm J_4^2(x^-)] F_{q-1}^2, \\
 \mu^\pm &= \frac{1}{4} \{ [J_2^2(x^+) \pm J_1^2(x^-)] F_q^2 + [J_1^2(x^+) \pm J_2^2(x^-)] F_{q+1}^2 \}, \\
 \delta^\pm &= \frac{1}{2} [J_2(x^+) J_5(x^+) \pm J_4(x^-) J_1(x^-)] F_{q-1} F_q, \\
 \theta^\pm &= \frac{1}{2} [J_5(x^+) J_1(x^+) \pm J_4(x^-) J_2(x^-)] F_{q-1} F_{q+1}, \\
 \psi^\pm &= \frac{1}{2} [J_2(x^+) J_1(x^+) \pm J_1(x^-) J_2(x^-)] F_q F_{q+1}. \quad (31)
 \end{aligned}$$



where $x^\pm = x_{q,q+1}^{(\pm)}$ are the arguments of the Bessel function. With these definitions, we can express the numerator and denominator of equation (15) defining the oscillating component $P_{q,q+1}$:

$$S_{q,q+1}^{(+)} \pm S_{q,q+1}^{(-)} = \gamma^\pm + \mu^\pm - \delta^\pm \cos(3\omega_{\text{NIR}}\tau + \varphi_q - \varphi_{q-1}) - \theta^\mp \cos(6\omega_{\text{NIR}}\tau + \varphi_{q+1} - \varphi_{q-1}) + \psi^\mp \cos(3\omega_{\text{NIR}}\tau + \varphi_{q+1} - \varphi_q). \quad (32)$$

The different functions are shown in figure 12 as a function of the field of the NIR pulse (F_{NIR}). We observe that only two terms (ψ^+ and μ^+) dominate up to a field amplitude $F_{\text{NIR}} \sim 0.006$ a.u., while the other two terms (ψ^- and μ^-) derived from one and two-photon transitions are negligible. For higher field strengths, the additional multi-NIR photon contributions (up to 4 and 5 photons) δ^\pm , γ^\pm and θ^\pm start playing a role. For fields as high as $F_{\text{NIR}} \sim 0.011$ – 0.012 a.u., the different contributions are comparable and the correlation plots present a complex pattern (not shown). At these high field strengths the correlation plots can no longer be described by ellipses.

5.3. Approximation III: $x_{q,q+1}^{(-)} \simeq x_{q,q+1}^{(+)} \rightarrow \Delta x_{q,q+1} = 0$

The last approximation used to derive the elliptical shape of the correlated sideband parameter is the assumption that the difference between the x -argument of the Bessel functions for consecutive sidebands is negligible:

$$\Delta x_{q,q+1} = \Delta x = \frac{x_{q,q+1}^{(+)} - x_{q,q+1}^{(-)}}{2} = 0.$$

We can perform a first order expansion around $\Delta x_{q,q+1} = 0$ to evaluate the effect of small variations of this parameter on the correlation plots. We define:

$$x_0 = \frac{x_{q,q+1}^{(+)} + x_{q,q+1}^{(-)}}{2},$$

and therefore:

$$x_{q,q+1}^{(+)} = x_0 + \Delta x, \quad x_{q,q+1}^{(-)} = x_0 - \Delta x.$$

Starting from the equations (13) and (15), the expression of the oscillating component of the sideband in the case of harmonics with equal amplitudes $F_q = F_{q+1}$ becomes:

$$P_{q,q+1}(x_0, \Delta x) = P_{q,q+1}(x_0, \Delta x = 0) \left\{ 1 - \Delta x \frac{2 \left[J_1^2(x_0) - J_2^2(x_0) - \frac{1}{x_0} J_1(x_0) J_2(x_0) \right]}{[J_1^2(x_0) + J_2^2(x_0)]} \cos \Phi \right\} + \Delta x \frac{2 [J_1^2(x_0) - 2J_2^2(x_0)]}{x_0 [J_1^2(x_0) + J_2^2(x_0)]}. \quad (33)$$

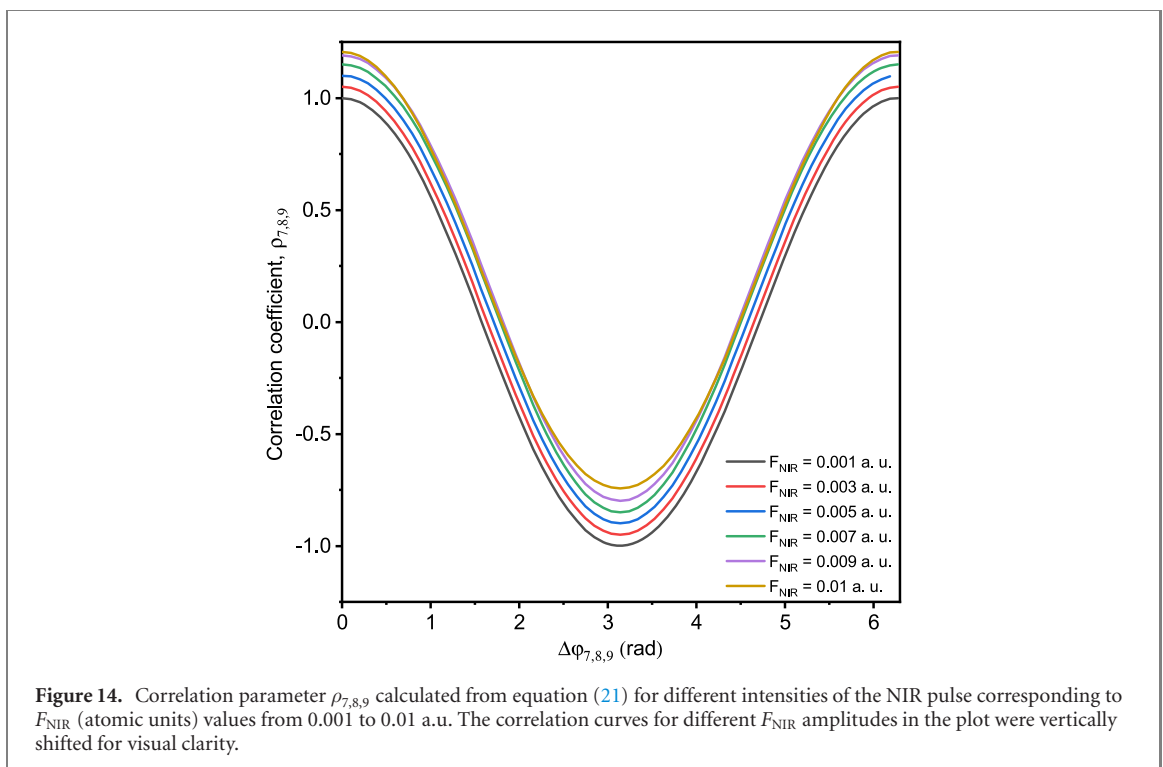
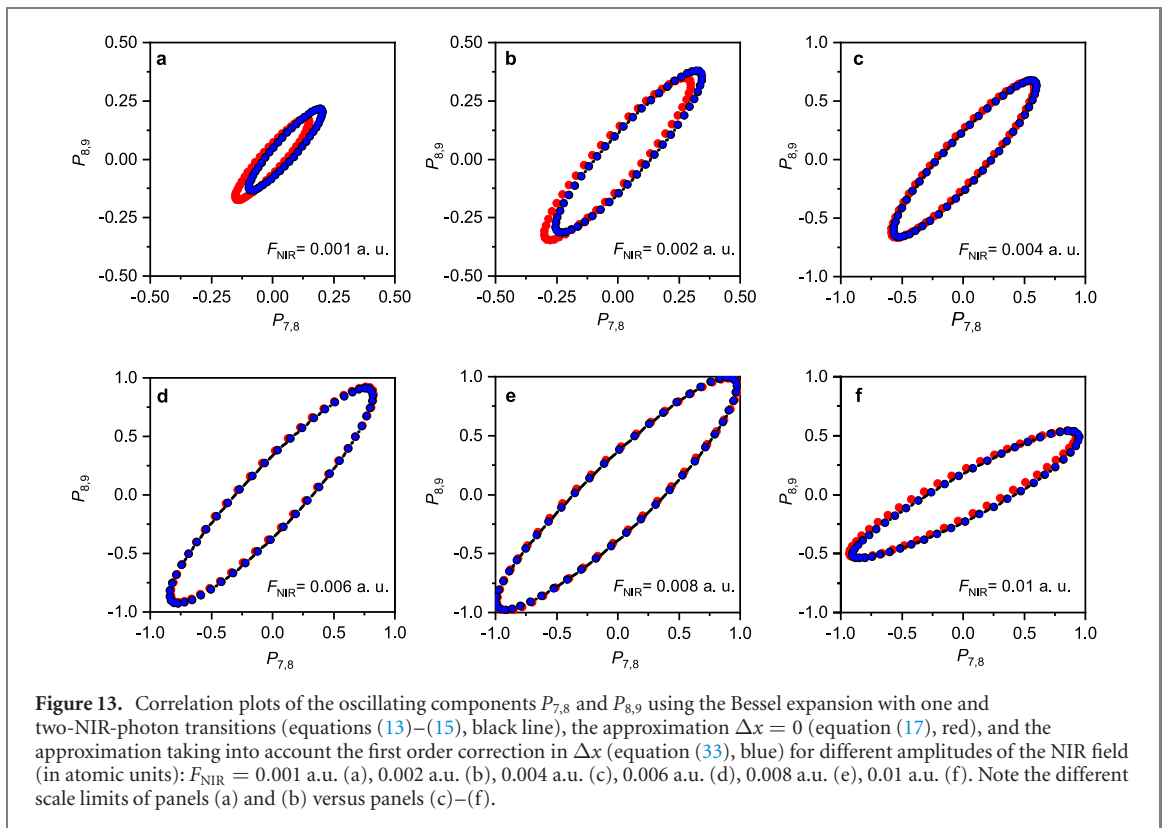


Figure 13 presents the comparison between the sideband correlated plot obtained for the approximation based on the Bessel expansion with one and two-NIR-photon transitions (black line), the approximation $\Delta x = 0$ (red), and the approximation taking the first order correction in Δx (blue). We can observe a very good agreement between the three curves for intensities F_{NIR} between 0.004 and 0.008 a.u.. At lower and higher NIR intensities, the importance of the first terms in Δx is more evident.

5.4. Intensity dependence of the correlation parameter $\rho_{q-1,q,q+1}$

Finally we evaluate the dependence of the correlation parameter $\rho_{q-1,q,q+1}$ derived for different NIR intensities from the sideband oscillations obtained from the complete integral (equation (10)). Figure 14 reports the correlation as a function of the phase difference $\Delta\varphi_{q-1,q,q+1}$ for different intensities of the NIR field. It is evident that the evolution of the correlation parameter is almost unaffected up to very large intensities. Even for the highest intensities, however, maximum positive (negative) correlation still corresponds to the condition $\Delta\varphi_{q-1,q,q+1} = 0$ ($\Delta\varphi_{q-1,q,q+1} = \pi$), as shown in figure 14.

The conclusion is that the correlation parameter is a very robust parameter, which maintains its validity for the reconstruction of the phase differences $\Delta\varphi_{q-1,q,q+1}$ even for those intensities for which the correlation plots start deviating significantly from the ellipses described by equation (20).

6. Conclusions

We investigated in detail the temporal characterization of trains of attosecond pulses generated at the seeded FEL FERMI. The analysis of the approximations indicates that the method based on the correlation analysis of the single-shot fluctuations of the sidebands can be applied over a large intensity range of the NIR field. The lower limit of this range is imposed by the single-shot detection of the sideband photoelectron signal and by the shot-to-shot fluctuations of the intensity of the single harmonics. The upper limit ($F_{\text{NIR}} \approx 0.008\text{--}0.009$ a.u.) is determined by the appearance of multi-NIR photon transitions (up to four and five-photon transitions). Nevertheless, even in a certain intensity range in which these transitions cannot be neglected the calibration procedure for the assignment of the phase difference of each setting of the phase shifters turns out to be reliable. Using this method, the complete phase and amplitude shaping of attosecond waveforms in time was demonstrated [22]. This approach outperforms other experimental approaches based on HHG sources and exploiting the dispersion of metallic filters [29, 30], the use of chirped mirrors [31], and the manipulation of the pulse structure and time-dependent polarization of the driving field [32–34]. The demonstration of sub-femtosecond pulses at FELs opens up new perspectives for the implementation of XUV-pump–XUV-probe approaches in the attosecond range [35, 36] and time-resolved coherent-control experiments in the XUV spectral range.

Acknowledgments

This project has received funding from the European Union’s Horizon 2020 research and innovation programme under the Marie Skłodowska-Curie Grant Agreement No. 641789 MEDEA. KU acknowledges support by the X-ray Free Electron Laser Utilization Research Project and the X-ray Free Electron Laser Priority Strategy Program of the Ministry of Education, Culture, Sports, Science and Technology of Japan (MEXT), by the Cooperative Research Program of ‘Network Joint Research Center for Materials and Devices: Dynamic Alliance for Open Innovation Bridging Human, Environment and Materials’, by the bilateral project CNR-JSPS ‘Ultrafast science with extreme ultraviolet Free Electron Laser’, and by the IMRAM project for the international co-operation. RF and RJS thank the Swedish Research Council (VR) and the Knut and Alice Wallenberg Foundation for financial support. SB, NI, ERS and JM thank the Swedish Research Council (VR) for support. AAL acknowledges support from the US Department of Energy contract DE-AC02-76SF00515. EVG acknowledges support of the Foundation for the Advancement of Theoretical Physics and Mathematics ‘BASIS’. Research at Louisiana State University was supported by the US Department of Energy, Office of Science, Basic Energy Sciences, under contract no. de-sc0010431. MM acknowledges support from the Deutsche Forschungsgemeinschaft (DFG) under Grant No. SFB925/A1. GS acknowledges funding from DFG, Project: 429805582. ANG and EVG acknowledge funding from the Russian Foundation for Basic Research (RFBR) under the Project No. 20-52-12023. GS acknowledges useful discussion about the simulations and the data analysis with Thomas Pfeifer and Matthias Kübel. We acknowledge L Foglia, A Simoncig, and M Coreno for valuable discussions.

Data availability statement

The data that support the findings of this study are available upon reasonable request from the authors.

ORCID iDs

P K Maroju  <https://orcid.org/0000-0003-1455-9051>

H Ahmadi  <https://orcid.org/0000-0003-1610-5811>
E Allaria  <https://orcid.org/0000-0001-9570-6361>
J Mauritsson  <https://orcid.org/0000-0002-7289-5072>
A N Grum-Grzhimailo  <https://orcid.org/0000-0003-1415-7327>
C Callegari  <https://orcid.org/0000-0001-5491-7752>

References

- [1] Krausz F and Ivanov M 2009 *Rev. Mod. Phys.* **81** 163
- [2] Callegari F, Sansone G, Stagira S, Vozzi C and Nisoli M 2016 *J. Phys. B: At. Mol. Opt. Phys.* **49** 062001
- [3] Carpeggiani P A et al 2014 *Phys. Rev. A* **89** 023420
- [4] Chatziathanasiou S et al 2017 *Photonics* **4** 26
- [5] Takahashi E J et al 2015 *IEEE J. Sel. Top. Quantum Electron.* **21** 801–55
- [6] Schulz S et al 2015 *Nat. Commun.* **6** 5938
- [7] Danailov M B et al 2014 *Opt. Express* **22** 012869
- [8] Zholents A A et al 2005 *Phys. Rev. Spec. Top.* **8** 040701
- [9] Thompson N R and McNeil B W J 2008 *Phys. Rev. Lett.* **100** 203901
- [10] Serkez S, Geloni G, Tomin S, Feng G, Gryzlova E V, Grum-Grzhimailo A N and Meyer M 2018 *J. Opt.* **20** 024005
- [11] Marinelli A, MacArthur J, Emma P, Guetg M, Field C, Kharakh D, Lutman A A, Ding Y and Huang Z 2017 *Appl. Phys. Lett.* **111** 151101
- [12] Duris J et al 2020 *Nat. Photon.* **14** 30
- [13] Huang S et al 2017 *Phys. Rev. Lett.* **119** 154801
- [14] Emma P et al 2010 *Nat. Photon.* **4** 641
- [15] Li S et al 2018 *Opt. Express* **26** 4531
- [16] Allaria E et al 2012 *Nat. Photon.* **6** 699
- [17] Prince K C et al 2016 *Nat. Photon.* **10** 176
- [18] Iablonskyi D et al 2017 *Phys. Rev. Lett.* **119** 073203
- [19] You D et al 2019 *New J. Phys.* **21** 113036
- [20] Giannessi L et al 2018 *Sci. Rep.* **8** 7774
- [21] Di Fraia M et al 2019 *Phys. Rev. Lett.* **123** 213904
- [22] Maroju P K et al 2020 *Nature* **578** 386
- [23] Paul P M et al 2001 *Science* **292** 1689
- [24] Finetti P et al 2017 *Phys. Rev. X* **7** 021043
- [25] Lewenstein M, Balcou P, Ivanov M Y, L’Huillier A and Corkum P B 1994 *Phys. Rev. A* **49** 2117
- [26] Kitzler M et al 2002 *Phys. Rev. Lett.* **88** 173904
- [27] Itatani J et al 2002 *Phys. Rev. Lett.* **88** 173903
- [28] Mairesse Y and Quéré F 2005 *Phys. Rev. A* **71** 011401
- [29] López-Martens R et al 2005 *Phys. Rev. Lett.* **94** 033001
- [30] Gustafsson E, Ruchon T, Swoboda M, Remetter T, Pourtal E, López-Martens R, Balcou P and L’Huillier A 2007 *Opt. Lett.* **32** 1353
- [31] Hofstetter M et al 2011 *Opt. Express* **19** 1767
- [32] Bartels R, Backus S, Zeek E, Misoguti L, Vdovin G, Christov I P, Murnane M M and Kapteyn H C 2000 *Nature* **406** 164
- [33] Sansone G 2009 *Phys. Rev. A* **79** 053410
- [34] Sansone G et al 2009 *Phys. Rev. A* **80** 063837
- [35] Makos I et al 2020 *Sci. Rep.* **10** 3759
- [36] Nayak A et al 2018 *Phys. Rev. A* **98** 023426